Stanford Exploration Project, Report 115, May 22, 2004, pages 199–213

Sensitivity kernels for wave-equation migration velocity analysis

Paul Sava and Biondo Biondi[1]

ABSTRACT

The success of migration velocity analysis methods is strongly dependent on the characteristics of the linearized tomographic operator that is inverted to estimate velocity updates. To study the properties of wave-equation migration velocity analysis, we analyze its sensitivity kernels. Sensitivity kernels describe the dependence of data space elements to small changes of model space elements. We show that the sensitivity kernels of wave-equation MVA depend on the frequency content of the recorded data and on the background velocity model. Sensitivity kernels computed assuming the presence of a salt body in the background velocity show that these kernels are drastically different from idealized "fat rays". Consequently sensitivity kernels cannot be approximated by artificial fattening of geometrical rays. Furthermore, our examples illustrate the potential of finite-frequency MVA as well as the frequency-dependent nature of illumination for subsalt regions.

INTRODUCTION

Depth imaging of complex structures depends on the quality of the velocity model. However, conventional Migration Velocity Analysis (MVA) procedures often fail when the wavefield is severely distorted by lateral velocity variations and thus complex multipathing occurs. Biondi and Sava (1999) introduce a method of migration velocity analysis using wave-equation techniques (WEMVA), which aims to improve the quality of migrated images, mainly by correcting moveout inaccuracies of specular energy. WEMVA finds a slowness perturbation which corresponds to an image perturbation. It is thus similar to ray-based migration tomography (Al-Yahya, 1989; Stork, 1992; Etgen, 1993), where the slowness perturbation is derived from depth errors, and to wave-equation inversion (Tarantola, 1986) or tomography (Woodward, 1992; Pratt, 1999; Dahlen et al., 2000) where the slowness perturbation is derived from measured wavefield perturbations.

WEMVA has the potential of improving velocity estimation when complex wave propagation makes conventional ray-based MVA methods less reliable. Imaging under rugged salt bodies is an important case where WEMVA has the potential of making a difference in the imaging results. In this paper, we analyze the characteristics of the tomographic operator inverted in WEMVA to update the velocity model, and contrast these characteristics with the

[1]**email:** paul@sep.stanford.edu, biondo@sep.stanford.edu

well-known characteristics of ray-based tomographic operators.

One way of characterizing integral operators, e.g. tomography operators, is through sensitivity kernels, which describe the sensitivity of a component of a member of the data space to a change of a component of a member of the model space. In this paper, we formally introduce the sensitivity kernels for wave-equation migration velocity analysis and show 2D and 3D examples.

The analysis of WEMVA sensitivity kernels provide an intuition on WEMVA's potential for overcoming limitations of ray-based MVA. Some of these limitations are intrinsic, other are practical. An important practical difficulty encountered when using rays to estimate velocity below salt bodies with rough boundaries is the instability of ray tracing. Rough salt topographies create poorly illuminated areas, or even shadow zones, in the subsalt region. The spatial distribution of these poorly illuminated areas is very sensitive to the velocity function. Therefore, it is often extremely difficult to trace the rays that connect a given point in the poorly illuminated areas with a given point at the surface (two-point ray-tracing). Wavefield-extrapolation methods are robust with respect to shadow zones and they always provide wavepaths (i.e. sensitivity kernels) usable for velocity inversion.

Ray-tracing has intrinsic limitations when modeling wave-propagation through salt bodies with complex geometry, because of the asymptotic assumption on which it is based. This intrinsic limitation prevent ray-tracing from modeling the frequency-dependency of full-bandwidth wave propagation. The comparison of sensitivity kernels computed assuming different frequency bandwidths illustrates clearly the drawbacks of the asymptotic assumptions. Top-salt rugosity causes the WEMVA sensitivity kernels to be strongly dependent on the bandwidth. Furthermore, in these conditions, sensitivity kernels are drastically different from simple "fat rays". Therefore, they cannot be approximated by kernels computed by a bandwidth-dependent fattening of geometric rays (Lomax, 1994).

We compute the sensitivity kernels for perturbations in the phase as well as perturbations in the amplitude. We observe that there is a 90 degree phase shift between these two types of kernels. It is interesting to notice that the 3-D kernels for phase perturbations are hollow in the middle, exactly where the geometric rays would be. This result is consistent with the observations first made by Woodward (1990); then extensively discussed in the global seismology community (Marquering et al., 1999; Dahlen et al., 2000), and further analyzed at SEP by Rickett (2000).

THEORY

Fréchet derivative integral kernels

Consider a (nonlinear) function $\mathbf{g}$ mapping one element of the functional model space $\mathbf{m}$ to one element of the functional data space $\mathbf{d}$:

$$\mathbf{d} = \mathbf{g}(\mathbf{m}) \ . \tag{1}$$

The tangent linear application to $\mathbf{g}$ at point $\mathbf{m} = \mathbf{m}_0$ is a linear operator $\mathbf{G}_0$ defined by the expansion

$$\mathbf{g}(\mathbf{m_0} + \delta\mathbf{m}) = \mathbf{g}(\mathbf{m_0}) + \mathbf{G_0}\delta\mathbf{m} + \dots \,, \tag{2}$$

where $\delta\mathbf{m}$ is a small perturbation in the model space. The tangent linear application $\mathbf{G}_0$ is also known under the name of *Fréchet derivative* of $\mathbf{g}$ at point $\mathbf{m}_0$ (Tarantola, 1987).

Equation (2) can be written formally as

$$\delta\mathbf{d} = \mathbf{G}_0\delta\mathbf{m} \,, \tag{3}$$

where $\delta\mathbf{m}$ is a perturbation in the model space, and $\delta\mathbf{d}$ is a perturbation in the image space. If we denote by δd^i the i^{th} component of $\delta\mathbf{d}$, and by $\delta m(\mathbf{x})$ an infinitesimal element of $\delta\mathbf{m}$ at location $\mathbf{x}$, we can write

$$\delta d^i = \int_{\mathcal{V}} G_0^i(\mathbf{x})\ \delta m(\mathbf{x})\ dv(\mathbf{x}) \ . \tag{4}$$

G_0^i is, by definition, the integral kernel of the Fréchet derivative $\mathbf{G}_0$, $\mathcal{V}$ is the volume under investigation, dv is a volume element of $\mathcal{V}$ and $\mathbf{x}$ is the integration variable over $\mathcal{V}$. The sensitivity kernel, a.k.a. *Fréchet derivative kernel*, G_0^i expresses the sensitivity of δd^i to a perturbation of $\delta m(\mathbf{x})$ for an arbitrary location $\mathbf{x}$ in the volume $\mathcal{V}$.

Sensitivity kernels occur in every inverse problem and have different meanings depending of the physical quantities involved:

- For **wideband traveltime tomography** (Bishop et al., 1985; Kosloff et al., 1996; Stork, 1992), $\delta\mathbf{d}$ is represented by traveltime differences between recorded and computed traveltimes in a reference medium. The sensitivity kernels are infinitely-thin rays computed by ray tracing in the background medium.

- For **finite-frequency traveltime tomography** (Marquering et al., 1999; Dahlen et al., 2000; Hung et al., 2000; Rickett, 2000), $\delta\mathbf{d}$ is represented by time shifts measured by crosscorelation between the recorded wavefield and a wavefield computed in a reference medium. The sensitivity kernels are represented by hollow fat rays (a.k.a. "banana-doughnuts") which depend on the background medium.

- For **wave-equation tomography** (Woodward, 1992; Pratt, 1999), $\delta\mathbf{d}$ is represented by perturbations between the recorded wavefield and the computed wavefield in a reference medium. The sensitivity kernels are represented by fat rays with similar forms for either the Born or Rytov approximation.

- For **wave-equation migration velocity analysis** (Biondi and Sava, 1999; Sava and Fomel, 2002; Sava and Biondi, 2004a,b), $\delta\mathbf{d}$ is represented by image perturbations. The sensitivity kernels are discussed in the following sections.

Wave-equation migration velocity analysis

Wave-equation migration velocity analysis (WEMVA) is based on a linear relation established between perturbations of the slowness model $\delta\mathbf{s}$ and perturbations of migrated images $\delta\mathbf{r}$. $\delta\mathbf{d}$ and $\delta\mathbf{r}$ correspond, respectively, to $\delta\mathbf{m}$ and $\delta\mathbf{d}$ in equation (3).

Formally, we can write

$$\delta\mathbf{r} = \mathbf{L}_0\delta\mathbf{s}\,, \tag{5}$$

where $\mathbf{L}_0$ is the linear first-order Born wave-equation MVA operator. The operator $\mathbf{L}_0$ incorporates all first-order scattering and extrapolation effects for media of arbitrary complexity. The major difference between WEMVA and wave-equation tomography is that $\delta\mathbf{d}$ is formulated in the image space for the former as opposed to the data space for the later. Thus, with WEMVA we are able to exploit the power of residual migration in perturbing migrated images – a goal which is much harder to achieve in the space of the recorded data.

By construction, the linear operator $\mathbf{L}_0$ depends on the wavefield computed by extrapolation of the surface data using the background slowness, which corresponds to $\mathbf{m}_0$ in equation (2). Thus, the operator $\mathbf{L}_0$ depends directly on the type of recorded data and its frequency content, and it also depends on the background slowness model. Thus, the main elements that control the shape of the sensitivity kernels are

- the frequency content of the background wavefield,
- the type of source from which we generate the background wavefield (e.g. point source, plane wave), and
- the type of perturbation introduced in the image space, which for this problem corresponds to the data space.

In our examples, we define two types of image perturbations: a purely kinematic type $\delta\mathbf{r}_k$, implemented simply as a derivative of the image with respect to depth, which can be implemented as a multiplication in the depth wavenumber domain (Sava and Biondi, 2004a,b) as follows:

$$\delta\mathbf{r}_k = -ik_z\mathbf{r}\,, \tag{6}$$

and a purely dynamic type $\delta\mathbf{r}_a$, implemented by scaling the reference image $\mathbf{r}$ with an arbitrary number:

$$\delta\mathbf{r}_a = \epsilon\mathbf{r}\,. \tag{7}$$

In both cases, the perturbations are limited to a small portion of the image. The main difference between $\delta\mathbf{r}_k$ and $\delta\mathbf{r}_a$ is given by the 90° phase-shift between the two image perturbations.

EXAMPLES

In our first example, we consider a background wavefield emerging from a fixed point source on the surface, but investigate the sensitivity kernels for various points in the image. Each panel in Figure 1 depicts a superposition of three elements: the velocity model, the band-limited wavefield corresponding to a point source on the surface, and the sensitivity kernel corresponding to a point in the subsurface.

A fundamental problem with ray-based MVA is that rays are poor approximations of the actual wavepaths when a band-limited seismic wave propagates through a rugose top of the salt. Figure 1 illustrates this issue quite clearly. It shows three sensitivity kernels for frequencies of $1-26$ Hz. The top panel in Figure 1 shows a wavepath that could be reasonably approximated using the method introduced by Lomax (1994) to trace fat rays using asymptotic methods. In contrast, the wavepaths shown in both the middle and bottom panels cannot be well approximated using Lomax' method. The amplitude and shapes of these wavepaths are much more complex than a simple fattening of a geometrical ray could ever describe. The bottom panel illustrates the worst situation for ray-based tomography because the rugosity of the top of the salt has the same scale as the spatial wavelength of the seismic wave.

The fundamental reason why the true wavepaths cannot be approximated using fattened geometrical rays is that they are frequency dependent. Figure 2 illustrates this dependency by depicting the wavepath shown in the bottom panel of Figure 1 as a function of the temporal bandwidth: $1-5$ Hz (top), $1-16$ Hz (middle), and $1-64$ Hz (bottom). The width of the wavepath decreases as the frequency bandwidth increases, and the focusing and defocussing of the energy varies with the frequency bandwidth.

In the next example (Figures 3 and 4) we compare the shapes of sensitivity kernels when we change the type of source for the background wavefield, its frequency content and the method used to generate an image perturbation in the subsurface. As for the preceding example, we show the results as a superposition of the velocity model, the background wavefield and the sensitivity kernel from a fixed point in the subsurface.

Figure 3 shows the sensitivity kernels for a point source on the surface, and Figure 4 shows the sensitivity kernels for a plane-wave propagating vertically at the surface. In both pictures, the left column corresponds to kinematic image perturbations of equation (6), and the right column corresponds to amplitude image perturbations of equation (7) obtained by scaling of the background image by an arbitrary number. From top to bottom, we show sensitivity kernels of increasing frequency range: $1-4$ Hz, $1-8$ Hz, $1-16$ Hz and $1-32$ Hz. Once again, we can see the large frequency dependence of the sensitivity kernels. The area of sensitivity reduces with increased frequency which is a clear indication that a frequency dependent migration velocity analysis method like WEMVA can better handle subsalt environments with patchy illumination and that illumination itself is a frequency dependent phenomenon which needs to be addressed in this way.

Finally, we show wave-equation MVA sensitivity kernels for a 3D velocity model Figure 5 corresponding to a salt environment. We consider the case of a point source on the surface and data with a frequency range of $1-16$ Hz. Figure 6 shows the sensitivity kernel for a kinematic

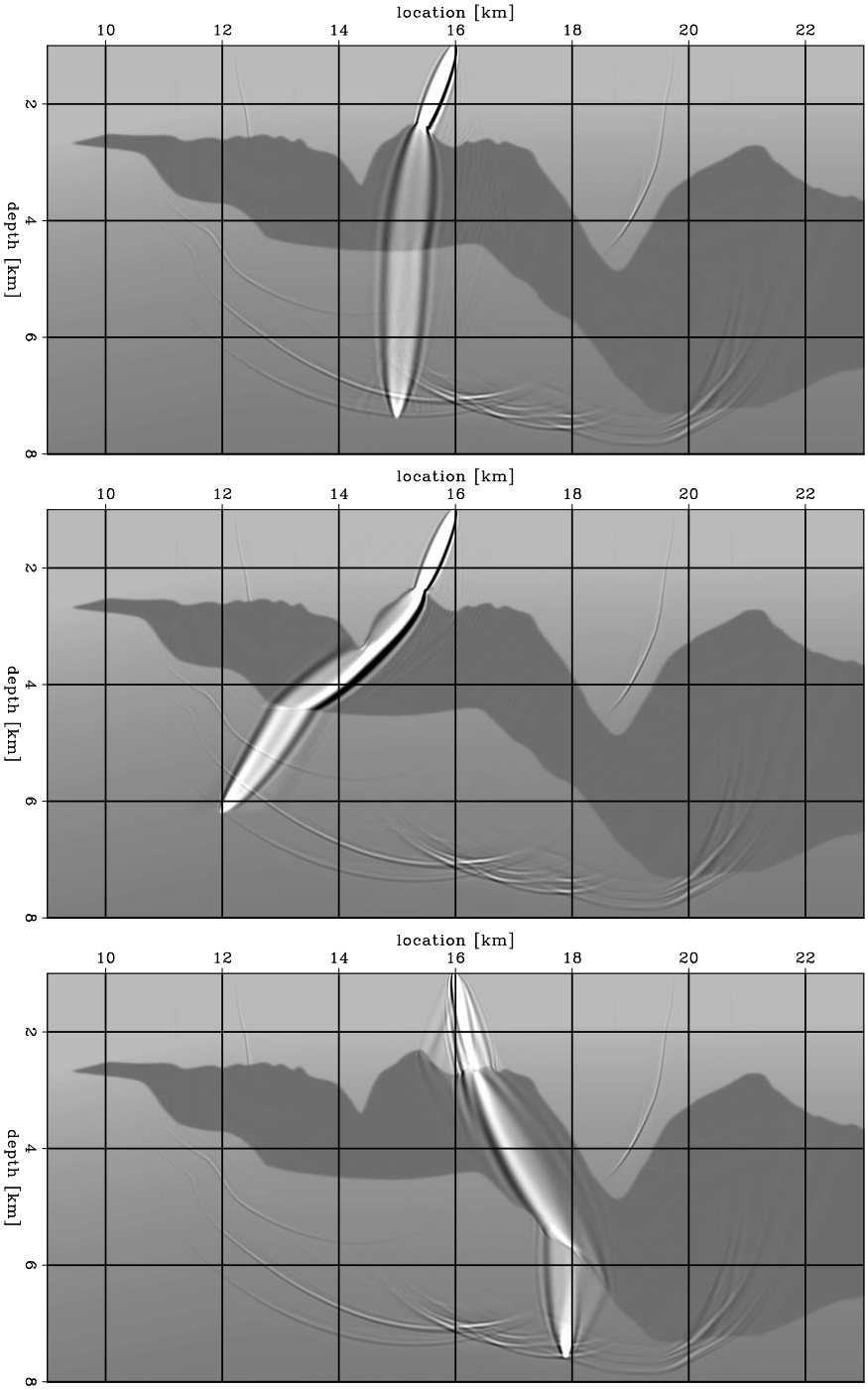

Figure 1: Kinematic sensitivity kernels for frequencies between 1 and 26 Hz for various locations in the image and a point on the surface. Each panel is an overlay of three elements: the slowness model, the wavefield corresponding to a point source on the surface at $x = 16$ km, and wave paths (sensitivity kernels) from a point in the subsurface to the source. paul1-zifat [CR]

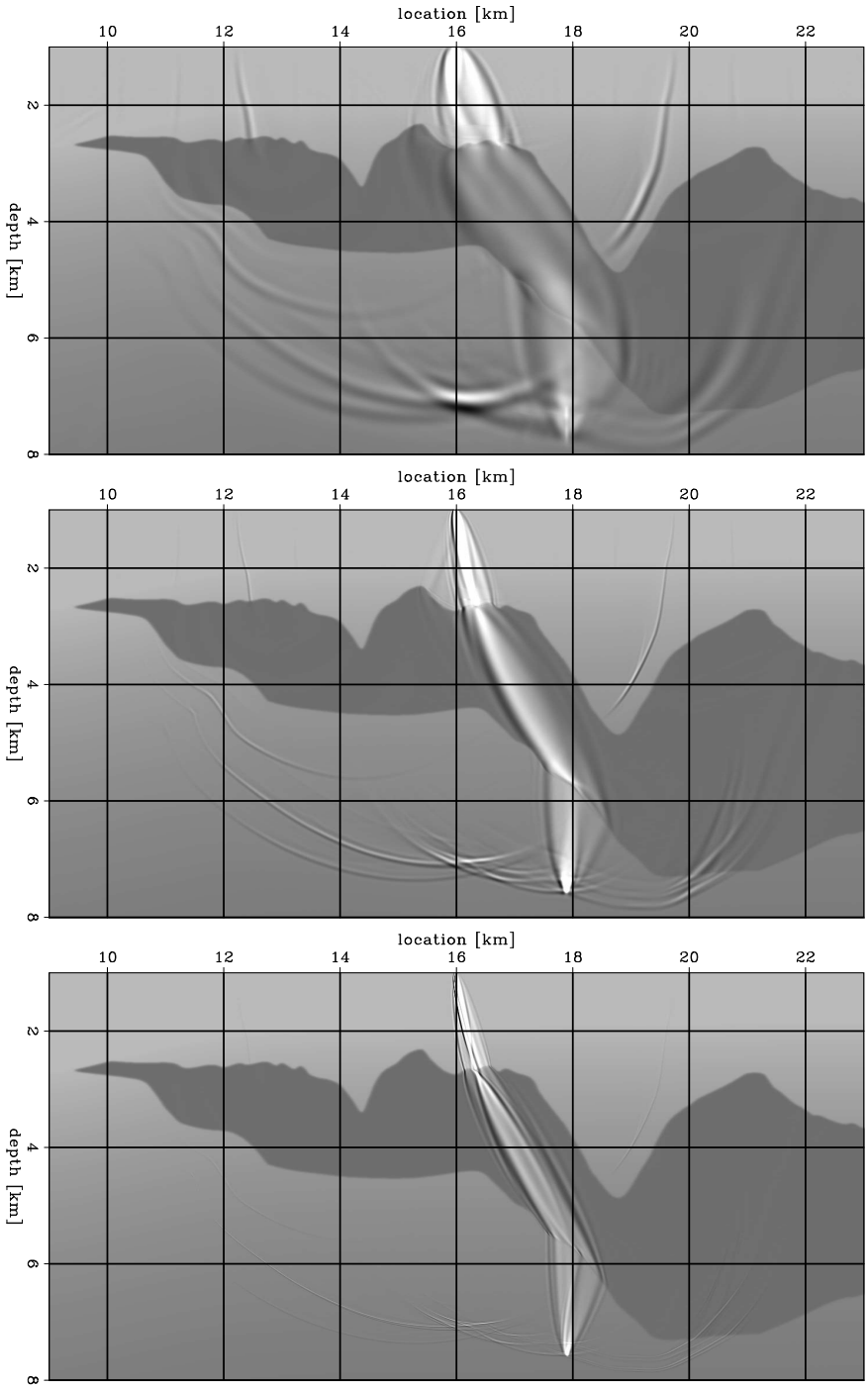

Figure 2: Frequency dependence of kinematic sensitivity kernels between a location in the image and a point on the surface. Each panel is an overlay of three elements: the slowness model, the wavefield corresponding to a point source on the surface at $x = 16$ km, and wave paths (sensitivity kernels) from a point in the subsurface to the source. The different wave paths correspond to frequency bands of $1-5$ Hz (top), $1-16$ Hz (middle) and $1-64$ Hz (bottom). The larger the frequency band, the narrower the wave path. The end member for an infinitely wide frequency band corresponds to an infinitely thin geometrical ray. paul1-zifrq2 [CR]

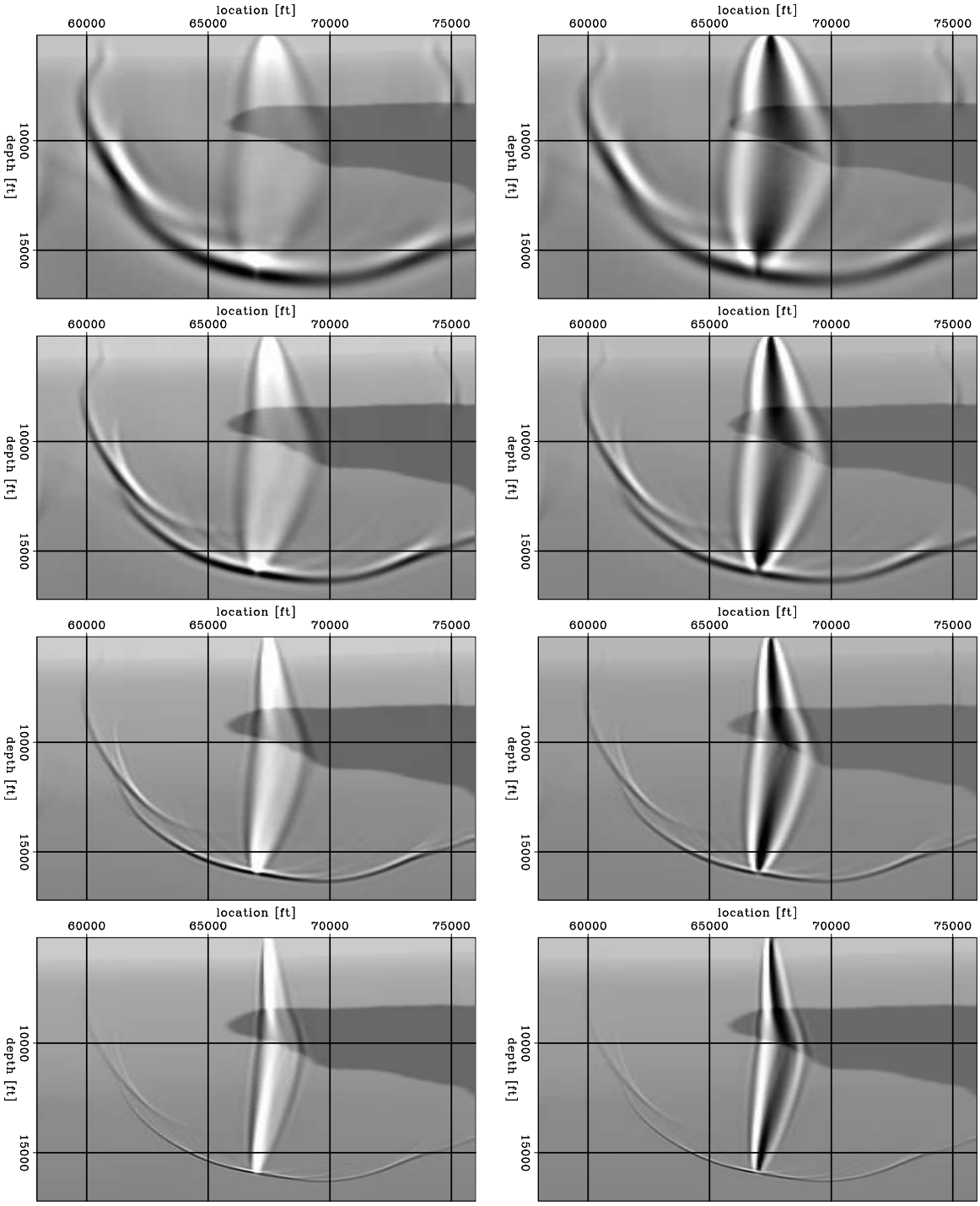

Figure 3: The dependence of sensitivity kernels to frequency and image perturbation. From top to bottom, the frequency range is $1-4$ Hz, $1-8$ Hz, $1-16$ Hz and $1-32$ Hz. The left column corresponds to kinematic image perturbations, and the right column corresponds to dynamic image perturbations. The wavefield is produced from a point source. paul1-fat2d.Tray2a [CR,M]

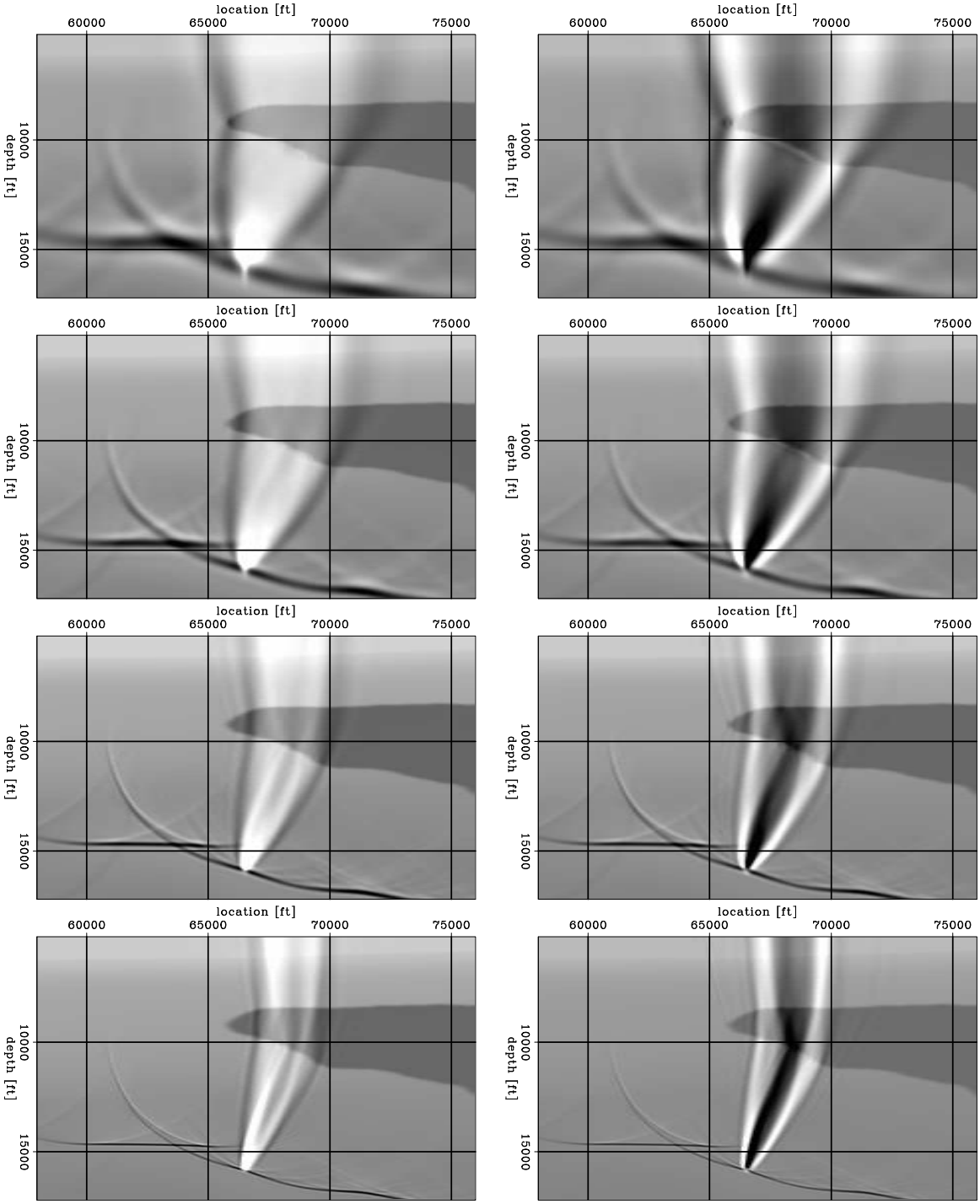

Figure 4: The dependence of sensitivity kernels to frequency and image perturbation. From top to bottom, the frequency range is $1-4$ Hz, $1-8$ Hz, $1-16$ Hz and $1-32$ Hz. The left column corresponds to kinematic image perturbations, and the right column corresponds to dynamic image perturbations. The wavefield is produced by a horizontal incident plane-wave. paul1-fat2d.Tray2b [CR,M]

image perturbation, while Figure 7 for a amplitude image perturbation. In both cases, the shapes of the kernels are complicated, which is an expression of the multipathing occurring as waves propagate through rough salt bodies. The horizontal slice indicates multiple paths linking the source point on the surface with the image perturbation in the subsurface.

One noticeable characteristic is that the sensitivity kernels constructed from amplitude image perturbations show the largest sensitivity in the center of the kernel, as opposed the kinematic kernels which show the largest sensitivity away from the central path. This phenomenon was discussed by Dahlen et al. (2000) in the context of finite-frequency traveltime tomography. We illustrate it for WEMVA in Figure 8 with two horizontal slices in the sensitivity kernels shown in Figures 6 and 7.

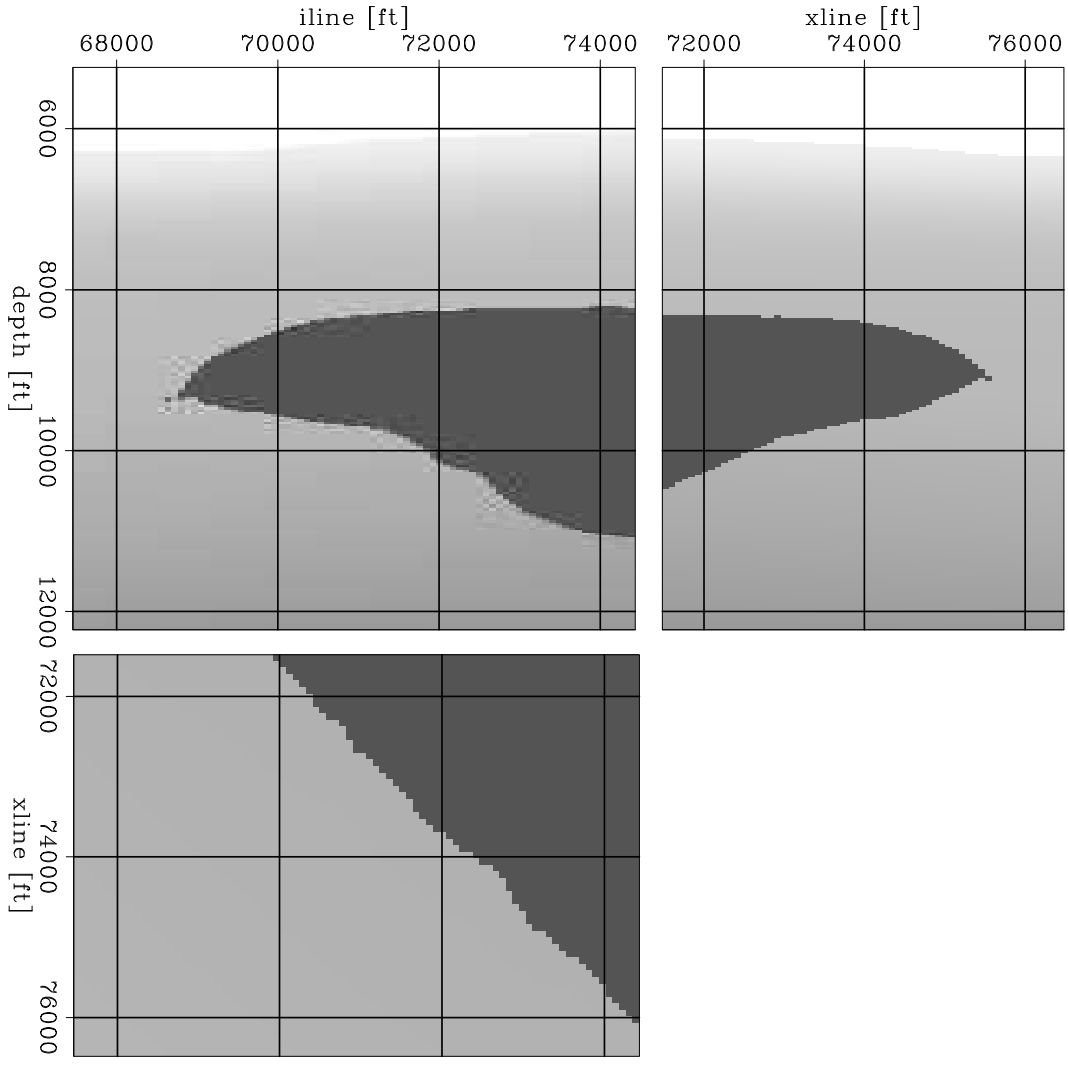

Figure 5: 3D slowness model. paul1-fat3.sC [CR]

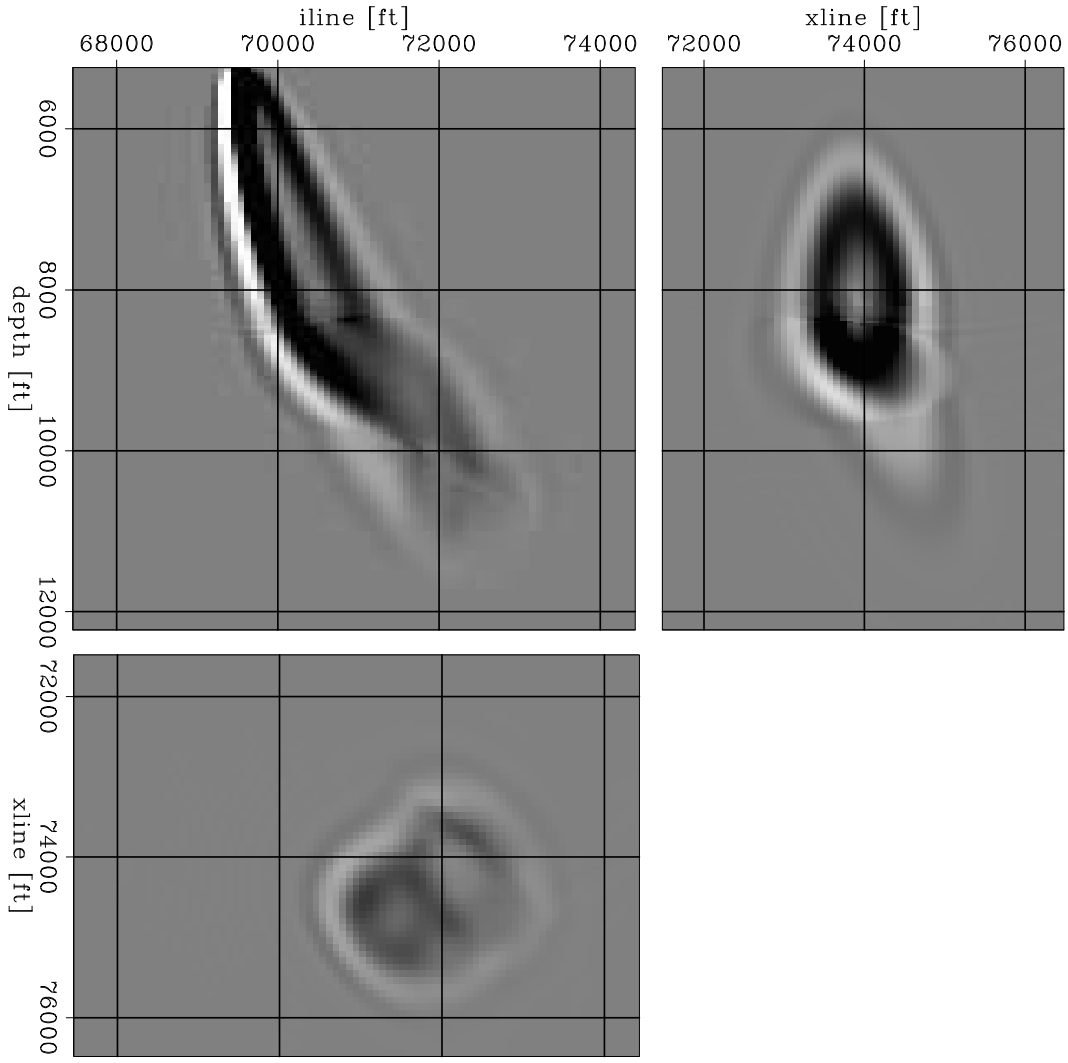

Figure 6: 3D sensitivity kernels for wave-equation MVA. The frequency range is $1 - 16$ Hz. The kernels are complicated by the multipathing occurring as waves propagate through the rough salt body. The image perturbation corresponds to a kinematic shift. paul1-fat3.fp3 [CR]

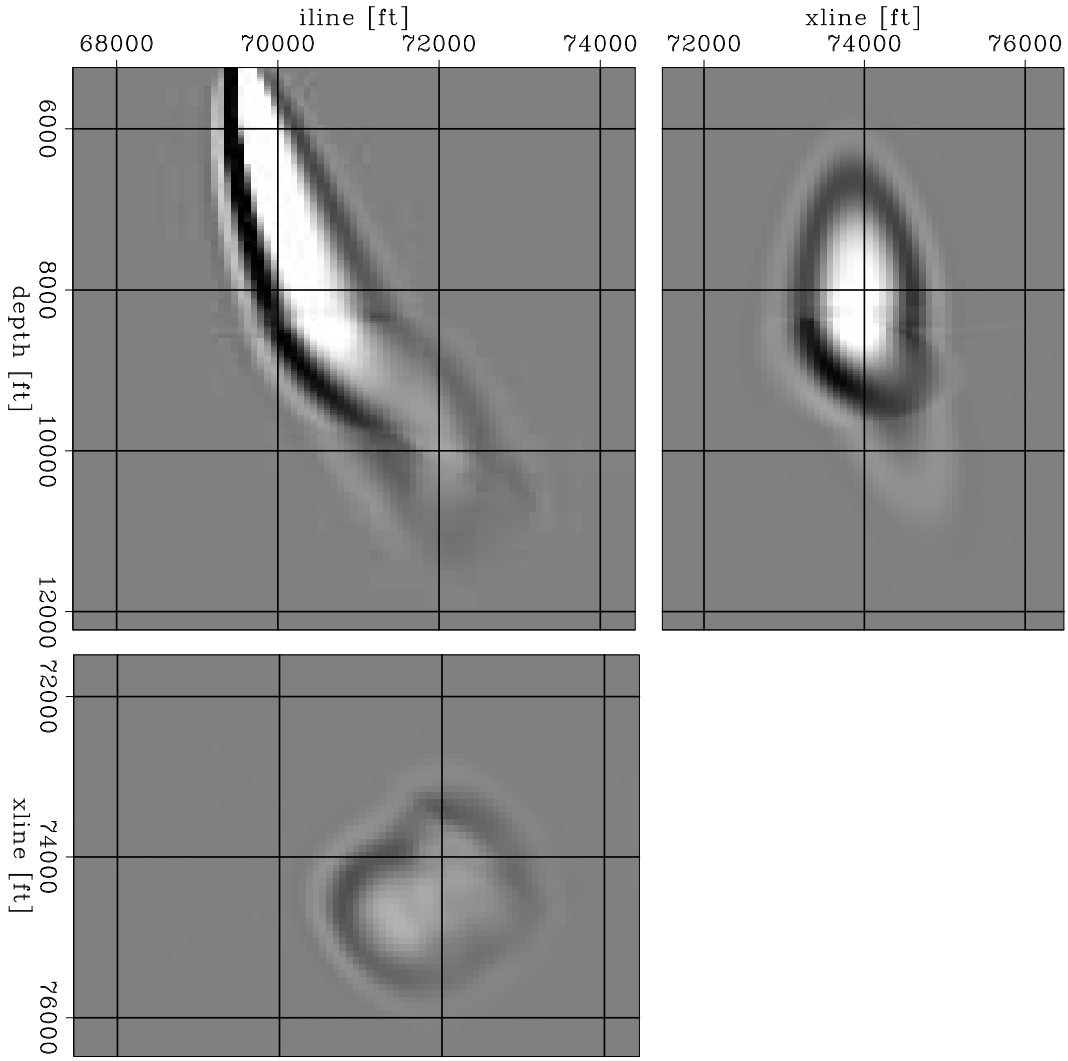

Figure 7: 3D sensitivity kernels for wave-equation MVA. The frequency range is $1 - 16$ Hz. The kernels are complicated by the multipathing occurring as waves propagate through the rough salt body. The image perturbation corresponds to an amplitude scaling. paul1-fat3.fq3 [CR]

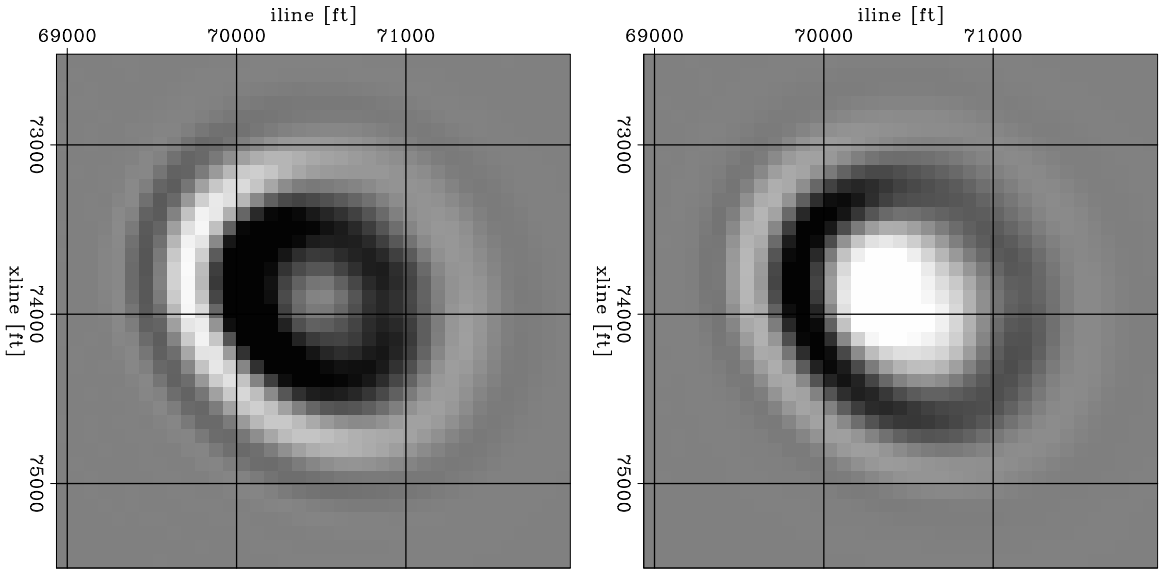

Figure 8: Cross-section of 3D sensitivity kernels for wave-equation MVA. The left panel corresponds to an image perturbation produced a kinematic shift, while the right panel corresponds to an image perturbation produced by amplitude scaling. The lowest sensitivity occurs in the center of the kinematic kernel (left). In contrast, the maximum sensitivity occurs in the center of the kernel (right). paul1-fat3.svty [CR]

CONCLUSIONS

We construct 2D and 3D sensitivity kernels for wave-equation MVA and study their dependence with respect to the data source, the frequency content, and the type of image perturbation. Sensitivity kernels illustrate the complications of wave propagation in the cases of rough salt bodies and the frequency-dependent illumination subsalt. With this type of analysis, we also illustrate some of the reasons why traveltime tomography is less than ideal for subsalt velocity analysis.

ACKNOWLEDGMENTS

We acknowledge BP and ExxonMobil for the 3D velocity model.

REFERENCES

Al-Yahya, K. M., 1989, Velocity analysis by iterative profile migration: Geophysics, **54**, no. 06, 718–729.

Biondi, B., and Sava, P., 1999, Wave-equation migration velocity analysis: Soc. of Expl. Geophys., 69th Ann. Internat. Mtg, 1723–1726.

Bishop, T. N., Bube, K. P., Cutler, R. T., Langan, R. T., Love, P. L., Resnick, J. R., Shuey, R. T., Spindler, D. A., and Wyld, H. W., 1985, Tomographic determination of velocity and depth in laterally varying media: Geophysics, **50**, no. 06, 903–923.

Dahlen, F. A., Hung, S. H., and Nolet, G., 2000, Frechet kernels for finite frequency traveltimes—I. Theory: Geophys. J. Int., **141**, 157–174.

Etgen, J. T., 1993, Interval velocity estimation using residual prestack migration: Soc. of Expl. Geophys., 63rd Ann. Internat. Mtg, 669–672.

Hung, S. H., Dahlen, F. A., and Nolet, G., 2000, Frechet kernels for finite frequency traveltimes—II. Examples: Geophys. J. Int., **141**, 175–203.

Kosloff, D., Sherwood, J., Koren, Z., MacHet, E., and Falkovitz, Y., 1996, Velocity and interface depth determination by tomography of depth migrated gathers: Geophysics, **61**, no. 05, 1511–1523.

Lomax, A., 1994, The wavelength-smoothing method for approximating broad-band wave propagation through complicated velocity structures: Geoph. J. Int., **117**, 313–334.

Marquering, H., Dahlen, F. A., and Nolet, G., 1999, Three-dimensional sensitivity kernels for finite-frequency traveltimes: the banana-doghnut paradox: Geophys. J. Int., **137**, 805–815.

Pratt, R. G., 1999, Seismic waveform inversion in the frequency domain, Part 1: Theory and verification in a physical scale model: Geophysics, **64**, no. 3, 888–901.

Rickett, J., 2000, Traveltime sensitivity kernels: Banana-doughnuts or just plain bananas?: SEP–**103**, 61–69.

Sava, P., and Biondi, B., 2004a, Wave-equation migration velocity analysis - I: Theory: submitted for publication in Geophysical Prospecting.

Sava, P., and Biondi, B., 2004b, Wave-equation migration velocity analysis - II: Subsalt imaging example: submitted for publication in Geophysical Prospecting.

Sava, P., and Fomel, S., 2002, Wave-equation migration velocity analysis beyond the Born approximation: Soc. of Expl. Geophys., 72nd Ann. Internat. Mtg, 2285–2288.

Stork, C., 1992, Reflection tomography in the postmigrated domain: Geophysics, **57**, no. 05, 680–692.

Tarantola, A., 1986, A strategy for nonlinear elastic inversion of seismic reflection data: Geophysics, **51**, no. 10, 1893–1903.

Tarantola, A., 1987, Inverse problem theory: Elsevier.

Woodward, M., 1990, Wave equation tomography: Ph.D. thesis, Stanford University.

Woodward, M. J., 1992, Wave-equation tomography: Geophysics, **57**, no. 01, 15–26.